

Moxibustion Spatial Transcriptomics Reveals Aqp4 Gene Distribution and Transport to the Astrocyte Endfeet Around Lateral White Matter of Hypothalamus (LWMH) are Potential Therapeutic Targets for Cognitive Impairment in APP/PS1 Mice

Shuqing Liu

Chengdu University of Traditional Chinese Medicine

Hongying Li

Chengdu University of Traditional Chinese Medicine

Yuan Shen

Chengdu University of Traditional Chinese Medicine

Weikang Zhu

Chinese Academy of Sciences

Yong Wang

Chinese Academy of Sciences

Junmeng Wang

Chengdu University of Traditional Chinese Medicine

Ning Zhang

Shanxi University of Traditional Chinese Medicine

Chenyu Li

Chengdu University of Traditional Chinese Medicine

Shuguang Yu

Chengdu University of Traditional Chinese Medicine

Lushuang Xie

Chengdu University of Traditional Chinese Medicine

Qiaofeng Wu (✉ wuqiaofeng@cducm.edu.cn)

Chengdu University of Traditional Chinese Medicine

Research Article

Keywords: Moxibustion, Alzheimer's disease, Spatial transcriptomics, Aquaporin-4, Myelin sheath

Posted Date: March 21st, 2022

DOI: <https://doi.org/10.21203/rs.3.rs-1458363/v1>

License:  This work is licensed under a Creative Commons Attribution 4.0 International License.

[Read Full License](#)

Abstract

Background

Aquaporin-4 (*Aqp4*), a predominantly aquaporin expressed on astrocytic endfeet, has been found to be potential targets for lymphatic clearance and transcytotic delivery in the disorder of glial lymphatic system and white matter fluid metabolism impairment such as Alzheimer's disease (AD). Moxibustion is an experience-based effective treatment for AD. Exploring the large amount of complex data of *Aqp4* in the processing of moxibustion may screen and provide accurate targets for prevention, ultimately leading to improve treatment options for AD.

Methods

The Morris water maze (MWM) was used to verify the effect of moxibustion on APP/PS1 mice. Wild type mice (WT) and APP/PS1 mice before and after treatment were used for spatial transcriptomics. *Aqp4* expression and perivascular polarization were quantified. Pathway enrichment was used to analyze the alteration of perivascular astrocytes and Lateral White Matter of Hypothalamus (LWMH). Immunofluorescence and transmission electron microscopy were used for protein level validation and myelin morphology observation, respectively.

Results

MWM testing showed an improved cognitive function of APP/PS1 mice treated with moxibustion. Among white matter regions, LWMH region of periventricular white matter was the most obvious change area of *Aqp4* gene in APP/PS1 mice, and moxibustion treatment can rescue this alteration. *Aqp4* mRNA and AQP4 protein located around the cerebral vessels of APP/PS1 mice decreased significantly ($P < 0.01$), especially in LWMH area. Moreover, the *Aqp4* mRNA transport capacity of astrocytes had a reduction ($P < 0.05$). Meanwhile, the ion transport function closely related to AQP4 in astrocytes was also disturbed. Finally, the abnormal expression of *Aqp4* and the imbalance of ion homeostasis in LWMH area, recovered after moxibustion, was closely related to the myelin injury.

Conclusion

Aqp4 polarized distribution in LWMH area was found to be the potential target for treating glial lymphatic disorder and white matter fluid metabolism impairment. Myelin damage in LWMH may be the following pathogenesis, which further decline the learning and memory ability such as AD.

Background

Glial lymphatic system disorder is the common pathological basis of many brain diseases such as Alzheimer's disease (AD) [1]. Previous imaging studies found that white matter altered in patients with mild cognitive impairment with the increasing of tau protein level in AD cerebrospinal fluid [2]. This may be due to the decrease of blood perfusion of deep white matter around the ventricle with the aging or progress of AD, resulting in hypoxia injury in this area [3] and axon injury or demyelination [4]. Further studies found that vascular permeability and fluid flow around cerebral vessels were mainly regulated by astrocytes which the membrane highly expresses aquaporin-4 (AQP4) [5, 6]. For instance, AQP4 is increasing in gray matter, decreasing in white matter, and ectopic around cerebral vessels in AD mice [7, 8]. The *Aqp4*^{-/-} APP/PS1 mice showed significantly decreased lymphatic flow rate and increased amyloid precipitation [9]. Thus, the change both in number and location of AQP4 may result in the accumulation or abnormal flow of liquid in the white matter area [8].

Moxibustion has been used to treat AD for many years, and has been proved to delay aging and improve cognitive impairment to a certain extent. Mechanism studies also show that moxibustion can prevent AD model by improving neuronal energy metabolism [10], inhibiting neuronal apoptosis, regulating the secretion of neural adhesion molecules [11], and promoting microglia polarization [12]. Then, does moxibustion have an effect on AQP4? Can it improve the changes of brain white matter in AD mice?

To investigate these issues, spatial transcriptomics (ST) was used in this study to analyze the changes of *Aqp4* gene in different brain areas and its distribution in perivascular astrocytes in APP/PS1 mice treated by moxibustion. Next, we will explore whether these changes are related to the myelin function of white matter which will finally demyelinated or targeted to the learning and memory ability in AD mice [13].

Methods

Animals

All experimental procedures were approved by the Animal Care and Use Committee of Chengdu University of Traditional Chinese Medicine (ethics number: 2018-10). All experimental mice were purchased from Cavens biogeo (suzhou) model animal research Co. Ltd. [license number: SCXK (su) 2018-0002], 5-month-old and weighed 28.0 ± 2 g. The WT mice were male C57BL/6J mice, while AD model mice were male APP/PS1 double transgenic mice. Mice were housed in a vivarium environment under a 12 h light-dark cycle (temperature $20 \pm 2^\circ\text{C}$, humidity 50–65%) and had free access to diet and drinking water. All the mice were screened by Morris water maze test after a week of adaptation. Then APP/PS1 mice were randomly divided into AD model group (APP/PS1) and moxibustion group (APP/PS1 + MOX), C57BL/6J mice were used as WT group.

Morris water maze (MWM) test

The MWM test was conducted in a circular tank (diameter, 90 cm; height, 30 cm) in a dimly lit room. The water temperature was kept at $22\text{--}25^\circ\text{C}$ to inhibit the mice from floating. A removable circular platform (9.5 cm in diameter, 28 cm in height) was equipped 1.5 cm below the milky water surface in one of the

quadrants. The pool area was divided into four equal quadrants and added markers in different shapes by affixing color cards. At four days visible platform training, each mouse received 4 training every day. Then at four consecutive days hidden platform training, mice were trained for four trials each day. After the last trial of training, all mice were given one probe trial for 90 s searching (probe trial) without platform. The time the mice spent in each quadrant was measured, in the meantime total swimming distance and crossing times in each quadrant were automatically recorded by water maze system (Chengdu Techman Software Co., Inc). See the experimental flow chart in Fig. 1a.

Moxibustion treatment

Treatments were performed after MWM test. Acupoints of “Yongquan” (KI1) and “Baihui” (GV20) were selected for intervention. Locations of the two acupoints were determined according to Government Channel and Points Standard GB12346-90 of China and “The Veterinary Acupuncture of China” (Fig. 1b). In APP/PS1 + MOX group, mice were treated with Moxa stick (diameter 0.5 cm, length 18 cm), which was ignited and hung 1.5 cm above acupoints. WT group and APP/PS1 group mice were only fastened without moxibustion. The treatment was 30-min per day and given consecutive five days every week for four weeks.

Sample Collection

After five days treatment and MWM test, all mice were anesthetized with 1% pentobarbital sodium (3 ml/kg). For ST, whole brains were isolated using aseptic technique and embedded in OCT and snap-frozen quickly. For immunofluorescence (IF), tissues were fixed in formaldehyde and embedded in paraffin. For transmission electron microscope (TEM), fresh brains were placed on the icebox and the optic tract was quickly stripped off. Then the optic tract tissues were cut to 2 mm³ and moved the tissues to the EP tube filled with fresh TEM fixative for further fixation.

Spatial transcriptomics (ST)

Sample preparation for spatial transcriptomics. The brains were cryosectioned coronally at a thickness of 10 μm by Cryostat Microtome (Leica CM3050, Germany). Then 5–10 sections were selected to be stained with HE, photographed and tested for RNA integrity number (RIN) value.

Spatial transcriptomics library preparation, sequencing and data pre-processing. The spatial transcriptomics libraries were prepared using the 10× Genomics Chromium system. Samples permeabilization was referred to Visium spatial tissue optimization kit (1000184, 10x Genomics, USA). After tissue permeabilization and cDNA synthesis, library preparation, and high-throughput sequencing, a total of 11,850 spots and about 1.7×10⁹ reads were targeted for capture from four mice samples. The raw data were processed using the analysis pipeline Space Ranger (1.0.0) for sample demultiplexing, barcode processing, reads alignment to mouse reference genome (mm10) and gene counting.

Spatial transcriptomics data analysis. After quality control in Seurat packages (v3.1.2), sample integration was done with using Space Ranger. Cell clustering, tSNE analysis, gene distribution analysis

and selection of subset were realized through Loupe Browser. Identification of cell types was based on known marker genes and a public mouse hippocampal single cell RNA-seq data set obtained through Gene Expression Omnibus (GEO) database[14]. The results of differentially expressed genes were obtained by selecting the data after merging and SCTtransform through Seurat packages, and having differential gene expression analysis through edgeR package (version 3.26.8). The pathway and process enrichment analyses were carried out by using Metascape [15].

Division of brain regions. The glia limitans layer selected the topmost spots of the cortex, the ependyma selected the spots around the ventricle, and the rest of the brain regions were selected according to the cell clusters and *The Mouse Brain in Stereotaxic Coordinates Third Edition* [16].

Screening methods for astrocyte adjacent to blood vessels. Astrocytes (AC) were selected as the intersection of spots with glial fibrillary acidic protein (*Gfap*) gene expression > 0 and *Aqp4* expression > 0 . The spots in the glia limitans region, ependymal region and choroid plexus region were eliminated from AC. BBB was selected as the intersection of spots with *Pecam1* expression > 0 and *Ft1* expression > 0 . And the spots in the choroid plexus region were eliminated from BBB. The above filtering method was implemented by software Loupe Browser. Then use the spatial information of the spots to filter out the adjacent AC and BBB for further analysis.

Methods for screening AC differentially expressed genes. The differentially expressed genes (DEGs) were screened with $|\text{Flod Change}| > 1.5$ and $p\text{-value adjust} < 0.05$. The screened DEGs was analyzed together with *Aqp4* during pathway enrichment.

Calculation of Aqp4 ratio. The *Aqp4* ratio in AC was the amount of *Aqp4* expression in adjacent BBB divided by the sum of *Aqp4* expression in AC and in BBB. The AC with multiple *Aqp4* ratios took the maximum value. The *Gfap* ratio was calculated according to the same method.

Selection method of the lateral white matter of hypothalamus (LWMH). LWMH was selected from the part of cluster 3 just below the fimbria.

Methods for screening AC differentially expressed genes. The DEGs were screened with $|\text{Flod Change}| > 1.5$ and adjusted $P(\text{Padj}) < 0.05$. Among them, the top 500 genes of APP/PS1 vs.WT sorted by *Padj* were used for gene enrichment.

Immunofluorescence (IF).

Briefly, brain tissues were sectioned into 10 μm thick slices. Sectioned samples were deparaffinized in xylene, rehydrated in a series of graded alcohol, and subjected to antigen retrieval. Endogenous peroxidase was quenched with 3.0% hydrogen peroxide in methanol for 30 min. Sections were further blocked with 3.0% bovine serum albumin (BSA) in PBS, exposed to 0.5% Triton X-100 for 1 hour for reducing nonspecific antibody binding and incubated with mouse AQP4 (ImmunoWay Biotechnology), rabbit MOG (Affinity Biosciences), or rabbit CD31 (Affinity Biosciences) antibody (1:200) at 4°C overnights. Then sections were washed with PBS three times and incubated with secondary antibody

(Alexa Fluor 488, cy3, Bioss, China, 1:200) for 2 hours at 37°C. Photographs were taken using an immunofluorescent microscope (Leica, Germany) and analyzed relative %area positive expression or average optical density with software Leica Application Suite X (Leica, Germany) and ImageJ.

Proportion of AQP4-coated cerebral vessels analysis. After immunofluorescence test, six 0.2mm * 0.2mm regions were randomly selected from the cerebral cortex of each sample. The blood vessels were the vacuoles with CD31 expression, and the positive expression of AQP4 was the first 1% fluorescence intensity in ImageJ software Threshold. The cerebral vessels surrounded by more than a quarter of AQP4 positive sites were the cerebral vessels co-labeled with AQP4. Finally, the proportion of cerebral vessels co-labeled with AQP4 in this region was calculated.

Transmission electron microscope (TEM).

After post-fixation for one week, brain tissues were washed by PBS, postfixed with 1% OsO₄ in PB at 4°C for 2 hours, dehydrated with graded acetone series, and stained with saturated uranyl acetate. After dehydration with graded acetone series again and embedded in Epon, ultrathin sections (60–70 nm) were cut by using an ultramicrotome (Leica UC7, Leica) and observed under a transmission electron microscope. Width of myelin sheath and diameter of axon were analyzed by ImageJ software. The g-ratio was calculated from 80 to 90 randomly selected myelinated axons each sample and measured as the axon diameter/total diameter of the axon plus the myelin sheath.

2.8 Statistical analysis.

Data are presented as the mean ± SD. Normality was tested with Shapiro-Wilk test. The behavioral data were analyzed by one-way repeated measures ANOVA. One-way ANOVA and Least-Significant Difference (LSD) were used to determine differences between groups. All data analysis was conducted using SPSS26.0 software (SPSS Inc., Chicago, USA) and GraphPad Prism 8 (GraphPad Prism Software Inc., San Diego, USA). $P < 0.05$ was considered statistically significant.

Results

Moxibustion could significantly improve the MWM test scores of APP/PS1 mice

In the MWM test, on the first day, there was little difference between APP/PS1 + MOX group and APP/PS1 group (Fig. 1c). But on the second day, the time for APP/PS1 + MOX mice to find the platform was shortened by 1/3, significantly different from that of APP/PS1 mice (Fig. 1c). In the later hidden platform stage, although the time for the three groups' mice to find the platform was continuously shortened, the training effect of APP/PS1 + MOX mice was significantly better than that of the APP/PS1 group (Fig. 1d). And in the final stage of removing the platform, the stay time in the target quadrant and the number of times crossing the platform in APP/PS1 + MOX group were significantly better than those in APP/PS1 group, but still could not reach the level in WT group (Fig. 1e-1f). This showed that the learning and

memory ability of APP/PS1 mice had been improved after moxibustion, but it had not reached the level of WT mice.

APP/PS1 mice has lower *Aqp4* gene, especially in the lateral white matter of hypothalamus (LWMH) area.

ST results showed that WT group and APP/PS1 group could be significantly separated in the T-SNE diagram. This meant the gene expression patterns of most cells in the mouse brain had changed in AD (Fig. 2a). After combining samples and graph-based clustering, 17 cell clusters were obtained (Fig. 2b). Combined with the location information of each cell cluster and a mouse brain atlas [16], we matched ten regions such as white matter, hippocampus 1, hippocampus 2, thalamus, hypothalamus 1, hypothalamus 2 and so on (Fig. 2c). Then we used edgeR for examining differential expression between APP/PS1 group and WT group and defined genes with $P_{adj} < 0.05$ and Fold Change > 1.5 or Fold Change < -1.5 as differentially expressed genes (DEGs). To identify the unique region-related DEGs, we used UpSet plot tool to make an intersection analysis and finally obtained 80 unique white matter-related DEGs (Fig. 2d). Among them, *Aqp4* ($\log_{2}FC = -0.73$, $P_{adj} = 1.56 \times 10^{-7}$) was used for further research, which is the key gene of glial-lymphatic system and BBB and plays an essential role in the disease progression of AD.

Subsequently, we analyzed the expression change of *Aqp4* in the whole brain and different regions. Results showed the number of high *Aqp4* expression spots (red spots) in APP/PS1 was significantly lower than those in WT group (Fig. 3a). The average level of *Aqp4* gene in APP/PS1 group was also significantly lower than that in WT group in whole brain (Fig. 3b, $P_{adj} = 7 \times 10^{-64}$) and most regions, such as hippocampus, thalamus, hypothalamus, cortex and white matter (Fig. 3e). Surprisingly, IF results showed that AQP4⁺ cells' mean fluorescence intensity tended to increase in whole brain (Fig. 3c-d, $P = 0.028$) and most regions, such as hippocampus, thalamus and glia limitans of brain surface (Fig. 3e) in APP/PS1 mice.

Considering that *Aqp4* is a white matter-related unique DEG, we directly analyzed the distribution difference of *Aqp4* gene in white matter by loupe browser soft. The results showed that *Aqp4* gene was highly expressed in the thalamus and perihypothalamic region of WT group, but perihypothalamic region lost the high expression level in APP/PS1 sample (Fig. 4a). However, this change of *Gfap*, which is also a gene marker of astrocytes, was not obvious (Fig. 4c). To further study this region, we annotated the spots with sequence data of single-cell transcriptome [13] (Fig. 4b) and combined with Allen Brain Atlas [17]. According to the gene expression data (Fig. 4d-4e), this region is mainly composed of oligodendrocytes and astrocytes with *Aqp4*. Because its distribution is closer to the lateral hypothalamus than the lateral ventricle, it was named lateral hypothalamic white matter (LWMH).

***Aqp4* decreased significantly in the perivascular astrocytes endfeet of APP/PS1 mice.**

Astrocytes extend feet encircle the abluminal side of the vessel and become an essential part of the blood-brain barrier (BBB). And microvascular flow is crucial for deep white matter [18]. To further analyze the *Aqp4* changes of the perivascular astrocytes in APP/PS1, the functioning astrocyte endfoot was evaluated as part of the BBB rather than the whole astrocyte. Based on this, we selected the BBB and its

surrounding astrocytes based on cell marker genes and cell spatial information (Fig. 5a). The results showed that the expression of *Aqp4* in perivascular astrocytes decreased in APP/PS1 group ($P < 0.01$), and this trend also existed in the BBB (Fig. 5b). And the number and proportion of perivascular astrocytes with high expression of *Aqp4* in the APP/PS1 group also decreased (Fig. 5c-5d), which powerfully illustrated the decrease of *Aqp4* expression around the cerebral vessels in AD.

GFAP is the major component of the intermediate filament cytoskeleton in astrocytes[19], the increase of its gene expression can represent the degree of astrocytes' size to some extent. In order to explore the relationship between AQP4 and volume state of astrocytes, we analyzed the correlation between *Aqp4* expression and *Gfap* expression in perivascular astrocytes. The result showed that APP/PS1 group's slope of the fitted line was lower than that of WT group, and the correlation between *Aqp4* and *Gfap* also decreased. (Fig. 5e, Pearson analysis, WT group: $R = 0.575$, $P < 1 \times 10^{-39}$; APP/PS1 group: $R = 0.363$, $P < 1 \times 10^{-8}$; merge: $R = 0.55$, $P < 1 \times 10^{-99}$) This means that *Aqp4* expression normally increases with the extension of astrocyte processes, but this correlation weakens in AD.

To study the changes of astrocytes around the BBB, differentially expressed genes analysis and gene pathway enrichment analysis were carried out (Supplementary Fig. 1a). The gene enrichment analysis using Metascape showed that pathways involved cytosolic ribosome, receptor ligand activity, postsynaptic density, ensheathment of neurons, axon, meal ion homeostasis and others (Fig. 5f). Among them, regulation of ion transport is closely related to AQP4, because AQP4 can regulate the endfoot membrane localization of ion channels via direct interaction[20, 21] (Fig. 5f-5g). And the myelin sheath suggested that the pathological changes of LWMH may be related to the pathological changes of astrocytes around BBB.

A study has shown that *Aqp4* and *Gfap* mRNA can be transported to the endfeet of astrocytes around the BBB and translated to form proteins[22]. And whether *Aqp4* mRNA distribution changes in AD astrocyte have not been verified. We used the proportion of BBB's *Aqp4* expression in astrocytes and BBB (*Aqp4* ratio) to indicate the ability of astrocytes to transport *Aqp4* mRNA (Fig. 6a). From the maps, it can be found that the number of astrocytes with *Aqp4* expressing near the BBB in APP/PS1 group was obviously less than that in WT group, and the average *Aqp4* ratio in APP/PS1 group significantly decreased (Fig. 6b, Flod Change = 0.86, $P < 0.05$).

In the separate analysis of LWMH region, we found that the difference in *Aqp4* ratio among groups was more obvious than that of the whole brain (Fig. 6c, Flod Change = 0.66, $P < 0.05$). And the number of BBB spots in LWMH decreased in APP/PS1 group (Fig. 6a, the amplified region).

In order to eliminate the effect of astrocytes endfeet loss on the *Aqp4* ratio, we carried out a correlation analysis. It was found that *Aqp4* ratio was almost unrelated to the proportion of *Gfap* in the BBB (Fig. 6c, Pearson analysis: $R = 0.19$, $P = 4.5 \times 10^{-14}$). It proved that the *Aqp4* ratio change in AD was not caused by the loss of astrocytes endfeet.

To verify this change of AQP4 around cerebral vessels at the protein level, we carried out co-labeled immunofluorescence of CD31 and AQP4. It was found that the proportion of AQP4-coated cerebral vessels in APP/PS1 group was significantly lower than that in WT group (Fig. 6e-6f, $P < 0.01$). This mRNA transport capacity decline has affected the normal function of AQP4.

The pathological changes in LWMH region of APP/PS1 mice may result in myelin damage.

The previous study showed that the change of *Aqp4* expression and *Aqp4* ratio in LWMH was the most obvious. To further study LWMH region, Allen Brain Explorer [23] was used to analyze the physiological structure located in LWMH region. The internal capsule, stria terminalis, auditory radiation and the optic tract were proved to be the main component of LWMH (Fig. 7a).

Then LWMH was extracted from cluster3 (Fig. 2b and 2c) of non-cerebral hemorrhage samples (Fig. 7b). Subsequently, we carried out differential gene expression analysis. A total of 151 up-regulated and 1643 down-regulated genes of APP/PS1 vs. WT were observed (Fig. 7c). Then we used the top 500 genes sorted by *Padj* for pathway enrichment analysis. Results showed that pathways were enriched in ribosome, electron transport chain, rRNA binding, myelin sheath, cellular responses to stimuli, ribosomal large subunit biogenesis, neuron to neuron synapse, and others (Fig. 7f). Among them, *Aqp4* participated in proton transmembrane transporter activity and transport of small molecules. It was worth noting that the myelin-related genes of the APP/PS1 mice changed, and LWMH was composed of nerve bundles that are responsible for transducing neural signals over long distances.

Then, to study the myelin change in APP/PS1 mice, we analyzed five myelin representative proteins in LWMH, and observed the differences among groups (Fig. 8a-8b). The results showed that the expression of *Plp1*, *Mbp*, *Pmp22*, *Mag* and *Mog* in APP/PS1 were indeed lower than that in WT. And the decrease of *Mag* expression in APP/PS1 was not significant, while the difference of *Plp1* among groups was the most significant.

In further study, we used IF to explore the expression and distribution of MOG and the relationship between AQP4 and LWMH. It was found that AQP4 was indeed heavily expressed in LWMH. Because of coronal sections, the most fluorescence profiles of AQP4 were strips or dots of fibrous astroglial processes rather than the shape of cellular bodies (Fig. 8c). The enlarged fluorescence picture showed that the fluorescence profile fragmentation of AQP4 in the APP/PS1 group was more serious than WT group (Fig. 8c). This indicated that the proportion of AQP4 in AD astrocyte processes decreased. In further analysis, the ratio of MOG and AQP4 in LWMH to whole brain showed a decreasing trend in APP/PS1, which meant that the myelin damage and low expression of AQP4 in this region were more serious than other brain regions in APP/PS1 mice (Fig. 8d-8e).

Finally, in order to further study the structural changes of myelin sheath, we performed transmission electron microscopy (TEM) analysis of the optic tract in mice. Compared to the WT mice, APP/PS1 mice exhibited degenerated sheaths, ballooned myelin, degenerated axons, and the loss of myelinated axons (Fig. 8f). Then quantitative TEM analysis revealed that APP/PS1 mice had significantly thinner myelin

than WT mice, which was reflected in the increase in the g-ratio (Fig. 8g). And the proportion of myelinated axons in all axons in APP/PS1 mice was lower than WT mice (Fig. 8h). It meant that there was obvious demyelination in LWMH of the APP/PS1 mice.

The changes of Aqp4 can be reversed by moxibustion to some extent

In spatial transcriptomics, compared with the APP/PS1 group, cell expression pattern of the APP/PS1 + MOX group was more similar to that of the WT group (Fig. 2a). In terms of *Aqp4* expression and enrichment in LWMH, the APP/PS1 mice after moxibustion treatment were also similar to those in the WT group (Fig. 2a and 3a). Moxibustion can significantly increase the expression of *Aqp4* in hippocampus, cortex, white matter, glia limitans of brain surface, thalamus and hypothalamus of APP/PS1 mice, but improve the increase of *Aqp4* expression in choroid plexus (Fig. 2d). It is interesting that although the protein level of AQP4 in APP/PS1 mice changed contrary to that of gene expression, moxibustion could still improve this change, especially in the hippocampus. In the study of perivascular astrocytes, moxibustion could increase the *Aqp4* expression (Fig. 5b-5d) and *Aqp4* ratio (Fig. 6a, 6b and 6d). The fitted line's slope and the correlation between *Aqp4* and *Gfap* in APP/PS1 mice's perivascular astrocytes also decreased after moxibustion. (Fig. 5e, Pearson analysis, APP/PS1 group: $R = 0.363$, $P < 1 \times 10^{-8}$; APP/PS1 + MOX group: $R = 0.618$, $P < 1 \times 10^{-37}$). Our IF experiments verified that moxibustion could improve the decrease of perivascular AQP4 in APP/PS1 mice (Fig. 6e-6f, $P < 0.01$). The number of LWMH's cerebral vessels and astrocytes expressing *Aqp4* around cerebral vessels also increased significantly after moxibustion (Fig. 6a). Thus, moxibustion could significantly improve the abnormal expression and the perivascular localization loss of AQP4, especially in LWMH.

The changes of AQP4 in astrocytes will cause a series of chain reactions. According to the relationship between up-regulated genes and down-regulated genes in different groups, we screened 279 key genes of moxibustion (Fig. 5i). The pathway enrichment analysis revealed that moxibustion can improve alteration of ion transmembrane transport, circadian misalignment and aberrant protein localization (Fig. 5j). Among the genes with altered ion transport function of perivascular astrocytes in APP/PS1 mice, which was related to AQP4, moxibustion can improve 60% genes of them (Fig. 5g-h).

In the analysis of LWMH, we selected 292 key genes of moxibustion (Fig. 7e). In pathway enrichment analysis of moxibustion key genes, the pathways were significantly enriched in myelin sheath and proton transmembrane transporter activity, which *Aqp4* participated in (Fig. 4g).

Finally, we found that moxibustion could improve the change of myelin protein in the LWMH (Fig. 8a and 8c) and the myelin shape and thickness changes shown by TEM in APP/PS1 mice (Fig. 8f-8g). Although the APP/PS1 + MOX group had relatively intact myelin shapes, there were still a large number of immature myelin sheaths, which may be caused by moxibustion promoting the renewal of myelin sheath (Fig. 8h).

Discussions

ST provided us with the changes of genes expression and distribution in the brain, and the effect of intervention could be shown on multi-sample clustering intuitively and effectively. However, 10X ST technology also has some shortcomings. The diameter of a spot in the 10X space transcriptomics chip is 55 microns, and the diameter of capillaries in the brain is between 5 and 10 microns. As a result, tiny structures such as the BBB cannot be isolated separately.

In this study, since one 10X ST spot may contain multiple small cells or cellular components. Thus, the BBB was not analyzed directly, but endothelial cells were used as the hallmark of BBB to locate the surrounding astrocytes (Fig. 9). On the other hand, the distance between the centers of the two spots is 100 microns in the 10X space transcriptomics chip, while the dendritic length of astrocytes can reach 90 microns[24]. So, we speculated that the ability of astrocytes to transport *Aqp4* mRNA to perivascular endfeet may be influenced in APP/PS1 mice since Boulay, A.C et al. reported *Aqp4* mRNA can be transported to the astrocytes endfeet [22]. Luckily, our ST results partially proved the above hypothesis.

Another possible issue of the increasing *Aqp4* in perivascular is caused by the co- location of blood vessels and astrocytes in one spot base on the ST data, but our further analysis denied this possibility because the correlation between *Gfap* and *Aqp4* in AC was strong (Fig. 5e) and the correlation between *Gfap* ratio and *Aqp4* ratio was weak (Fig. 6d).

Our IF result of AQP4 protein expression was consistent with some studies which also found that AQP4 had increased in both AD patients and AD model animals [25, 26]. However, in our ST data, the expression of *Aqp4* was on the opposite trend in APP/PS1 mice. Initially, we thought it was an error. But in the moxibustion group, we found moxibustion improved the level of *Aqp4* and the content of AQP4, indicating this opposite trend in APP/PS1 mice was a pathological change. As mentioned above, we guessed this phenomenon may also be caused by the perivascular astrocytes' ability of transporting *Aqp4* mRNA to the endfeet in APP/PS1 mice. So, we calculated the proportion of *Aqp4* ratio in different parts of astrocytes. From the box diagram of *Aqp4* ratio (Fig. 6b-c), we can see that moxibustion can significantly increase the proportion of *Aqp4* in the endfeet of astrocytes. Comprehensively, we speculated that the APP/PS1 mice could unable to transport *Aqp4* mRNA to the endfeet normally, resulting in a large amount of AQP4 aggregation in the cell body. Then, due to negative feedback, *Aqp4* mRNA decreased in transcriptional level. Of course, the above analysis needs further verification.

LWMH is located between the lateral ventricle and hypothalamus, where has a large amount of liquid by Nuclear Magnetic Resonance Imaging (MRI) detection, indicating a large amount of *Aqp4* in LWMH [2]. Previous study showed that patients with AD had less AQP4 in the white matter than normal people, which was closely related to the decreased clearance function of the glial lymphoid system in AD [27]. Therefore, the current study accurately located the region in the white matter.

When exploring the relationship between the AQP4 changes and the alteration of LWMH, we found the expression of *Aqp4*, the number of cerebral vessels and perivascular *Aqp4* localization in LWMH decreased in the APP/PS1 mice. These changes may decrease blood perfusion and fluid flow rate in LWMH, resulting in an anoxic environment and oxidative stress. In the previous analysis of perivascular

astrocytes, it was found that there was a disturbance of ion transport in perivascular astrocytes in APP/PS1 group. AQP4 and Kir4.1 are co-localized in astrocyte membranes [28] and associate with the mechanosensitive cation channel TRPV4 [29], which is known to mediate Ca^{2+} influx. Considering a large number of fibrous astrocytes and the closed fluid space exist in the white matter, it is not difficult to infer that ion homeostasis will occur in the white matter region due to the loss of normally expressed AQP4 on the astrocyte membrane. The oxidative stress and ion homeostasis imbalance, which will make myelin sheath damage[30], can be verified by the differential gene pathways enrichment of LWMH. Therefore, we inferred that myelin damage would be happen due to hypoxia and ion imbalance in the LMWH mediated by AQP4 in APP/PS1 mice.

To confirm our inference, TEM test was carried out. The results showed moxibustion could significantly improve the thickness of the myelin sheath. And the proportion of immature myelin in the APP/PS1 mice treated with moxibustion was higher (Fig. 8h), which suggested that the mechanism of moxibustion in improving myelin injury is enhancing myelin renewal. Combined with the effect of transport of *Aqp4* mRNA in astrocytes on myelin sheath discussed earlier, we believe that LWMH is moxibustion target to improve the transport of *Aqp4* mRNA in astrocytes, relieve the hypoxia environment and ion homeostasis disorder in LWMH, and promote the renewal of myelin sheath.

Conclusion

To sum up, the enhancement of transport *Aqp4* mRNA to astrocytes endfeet in LWMH area is a key mechanism of moxibustion to improve the cognitive function in APP/PS1 mice. This founding inspires us to develop new therapeutic measures at *Aqp4* and LWMH to treat AD and other glial lymphatic system disorder and white matter fluid metabolism impairment.

Abbreviations

AQP4
Aquaporin-4
MWM
Morris water maze
WT
Wild type
LWMH
Lateral White Matter of Hypothalamus
AD
Alzheimer's disease
ST
Spatial transcriptomics
IF
Immunofluorescence

TEM
Transmission electron microscope
RIN
RNA integrity number
GEO
Gene Expression Omnibus
Padj
adjusted *P*
AC
Astrocytes
DEGs
Differentially expressed genes
LSD
Least-Significant Difference
Gfap
Glial fibrillary acidic protein
BBB
Blood-brain barrier
MRI
Magnetic Resonance Imaging.

Declarations

Ethics approval and consent to participate

All experimental procedures were approved by the Animal Care and Use Committee of Chengdu University of Traditional Chinese Medicine (ethics number: 2018-10). All experimental mice were purchased from Cavens biogle (suzhou) model animal research Co. Ltd. [license number: SCXK (su) 2018-0002].

Consent for publication

Not applicable.

Availability of data and materials

The dataset used and/or analyzed during the current study are available from the corresponding author on reasonable request.

Competing interests

The authors declare that they have no competing interests.

Funding

This work was supported by the National Natural Science Foundation of China (No. 82174512, 82174511, 81873383). the National Key R&D Program of China (No.2019YFC1709001); Innovation Team and Talents Cultivation Program of National Administration of Traditional Chinese Medicine. (No: ZYYCXTD-D-202003), and Fund of Science and Technology Department of Sichuan Province, China (No.2021ZYD0081).

Authors' contributions

SL, HL, QW and LX drafted the paper; SY and QW conceived and designed the experiments; SL, HL, YS, JW, NZ, CL, LX performed the experiments; SL, WZ, YW and QW analyzed the images and data. All authors read and approved the final manuscript. SL and HL contributed equally to this work.

Acknowledgements

We would like to thank Jiayi Sun at Institute of Chinese Medicine and Pharmacy, Chengdu University of Traditional Medicine, for the assistance with confocal laser scanning microscopy.

References

1. Knopman DS, Jagust WJ. Alzheimer Disease Spectrum: Syndrome and Etiology From Clinical and PET Imaging Perspectives. *Neurology*. 2021;96(7):299–300.
2. Tosto G, Zimmerman ME, Hamilton JL, Carmichael OT, Brickman AM. The effect of white matter hyperintensities on neurodegeneration in mild cognitive impairment. *Alzheimers Dement*. 2015;11(12):1510–1519.
3. Schuff N, Matsumoto S, Kmiecik J, et al. Cerebral blood flow in ischemic vascular dementia and Alzheimer's disease, measured by arterial spin-labeling magnetic resonance imaging. *Alzheimers Dement*. 2009;5(6):454–462.
4. Prins ND, Scheltens P. White matter hyperintensities, cognitive impairment and dementia: an update. *Nat Rev Neurol*. 2015;11(3):157–165.
5. Chapouly C, Tadesse Argaw A, Horng S, et al. Astrocytic TYMP and VEGFA drive blood-brain barrier opening in inflammatory central nervous system lesions. *Brain*. 2015;138(Pt 6):1548–1567.
6. Mestre H, Hablitz LM, Xavier AL, et al. Aquaporin-4-dependent glymphatic solute transport in the rodent brain. *Elife*. 2018;7.
7. Kress BT, Iliff JJ, Xia M, et al. Impairment of paravascular clearance pathways in the aging brain. *Ann Neurol*. 2014;76(6):845–861.
8. Owasil R, O'Neill R, Keable A, et al. The Pattern of AQP4 Expression in the Ageing Human Brain and in Cerebral Amyloid Angiopathy. *Int J Mol Sci*. 2020;21(4):1225.

9. Xu Z, Xiao N, Chen Y, et al. Deletion of aquaporin-4 in APP/PS1 mice exacerbates brain A β accumulation and memory deficits. *Mol Neurodegener*. 2015;10:58–58.
10. Liu Q. *Energy transportation-mediated enhancement of synaptic plasticity in hippocampal neurons of SAMP8 by acupuncture*, Chengdu University of traditional chinese medicine; 2015.
11. Shengfeng LU XS, Yong TANG,Haiyan Yin,Jin Cheng,Shuguang Yu. Effects of electroacupuncture on neural cell adhesion of synaptic plasticity in the hippocampus of SAMP8. *Chinese Journal of Rehabilitation Medicine*. 2008;23(12):1057–1060% @ 1001–1242%L 1011–2540/R %W CNKI.
12. XIE Lu-shuang WQ-f, TANG Yong, ZHUANG Zhi-qi, ZHAO Na, HUANG Biao, YU Shu-guang. Study on electroacupuncture promoting the polarization of M2 phenotype microglia cells in hippocampus of AD model rats. *CHINESE ARCHIVES OF TRADITIONAL CHINESE MEDICINE*. 2018;33(5):1816–1820.
13. Coltman R, Spain A, Tsenkina Y, et al. Selective white matter pathology induces a specific impairment in spatial working memory. *Neurobiol Aging*. 2011;32(12):2324.e2327-2312.
14. Butt UJ, Steixner-Kumar AA, Depp C, et al. Hippocampal neurons respond to brain activity with functional hypoxia. *Mol Psychiatry*. 2021;26(6):1790–1807.
15. Zhou Y, Zhou B, Pache L, et al. Metascape provides a biologist-oriented resource for the analysis of systems-level datasets. *Nat Commun*. 2019;10(1):1523–1523.
16. Franklin K, Paxinos G. *The Mouse Brain in Stereotaxic Coordinates*. Elsevier Academic Press. 2007.
17. Lein ES, Hawrylycz MJ, Ao N, et al. Genome-wide atlas of gene expression in the adult mouse brain. *Nature*. 2007;445(7124):168–176.
18. Koizumi K, Hattori Y, Ahn SJ, et al. Apo ϵ 4 disrupts neurovascular regulation and undermines white matter integrity and cognitive function. *Nat Commun*. 2018;9(1):3816–3816.
19. Hol EM, Pekny M. Glial fibrillary acidic protein (GFAP) and the astrocyte intermediate filament system in diseases of the central nervous system. *Curr Opin Cell Biol*. 2015;32:121–130.
20. Rakers C, Schmid M, Petzold GC. TRPV4 channels contribute to calcium transients in astrocytes and neurons during peri-infarct depolarizations in a stroke model. *Glia*. 2017;65(9):1550–1561.
21. Tosun C, Kurland DB, Mehta R, et al. Inhibition of the Sur1-Trpm4 channel reduces neuroinflammation and cognitive impairment in subarachnoid hemorrhage. *Stroke*. 2013;44(12):3522–3528.
22. Boulay AC, Saubaméa B, Adam N, et al. Translation in astrocyte distal processes sets molecular heterogeneity at the gliovascular interface. *Cell Discov*. 2017;3:17005.
23. Lau C, Ng L, Thompson C, et al. Exploration and visualization of gene expression with neuroanatomy in the adult mouse brain. *BMC Bioinformatics*. 2008;9:153.
24. Lange J, Haslett LJ, Lloyd-Evans E, et al. Compromised astrocyte function and survival negatively impact neurons in infantile neuronal ceroid lipofuscinosis. *Acta Neuropathol Commun*. 2018;6(1):74–74.
25. Moftakhar P, Lynch MD, Pomakian JL, Vinters HV. Aquaporin expression in the brains of patients with or without cerebral amyloid angiopathy. *J Neuropathol Exp Neurol*. 2010;69(12):1201–1209.

26. Zhang J, Zhan Z, Li X, et al. Intermittent Fasting Protects against Alzheimer's Disease Possible through Restoring Aquaporin-4 Polarity. *Front Mol Neurosci.* 2017;10:395–395.
27. Owasil R, O'Neill R, Keable A, et al. The Pattern of AQP4 Expression in the Ageing Human Brain and in Cerebral Amyloid Angiopathy. *Int J Mol Sci.* 2020;21(4).
28. Nagelhus EA, Mathiesen TM, Ottersen OP. Aquaporin-4 in the central nervous system: cellular and subcellular distribution and coexpression with KIR4.1. *Neuroscience.* 2004;129(4):905–913.
29. Benfenati V, Caprini M, Dovizio M, et al. An aquaporin-4/transient receptor potential vanilloid 4 (AQP4/TRPV4) complex is essential for cell-volume control in astrocytes. *Proc Natl Acad Sci U S A.* 2011;108(6):2563–2568.
30. Nasraby SE, Rizvi B, Goldman JE, Brickman AM. White matter changes in Alzheimer's disease: a focus on myelin and oligodendrocytes. *Acta Neuropathol Commun.* 2018;6(1):22.

Supplementary Figures

Supplementary Figure 1a is not available with this version

Figures

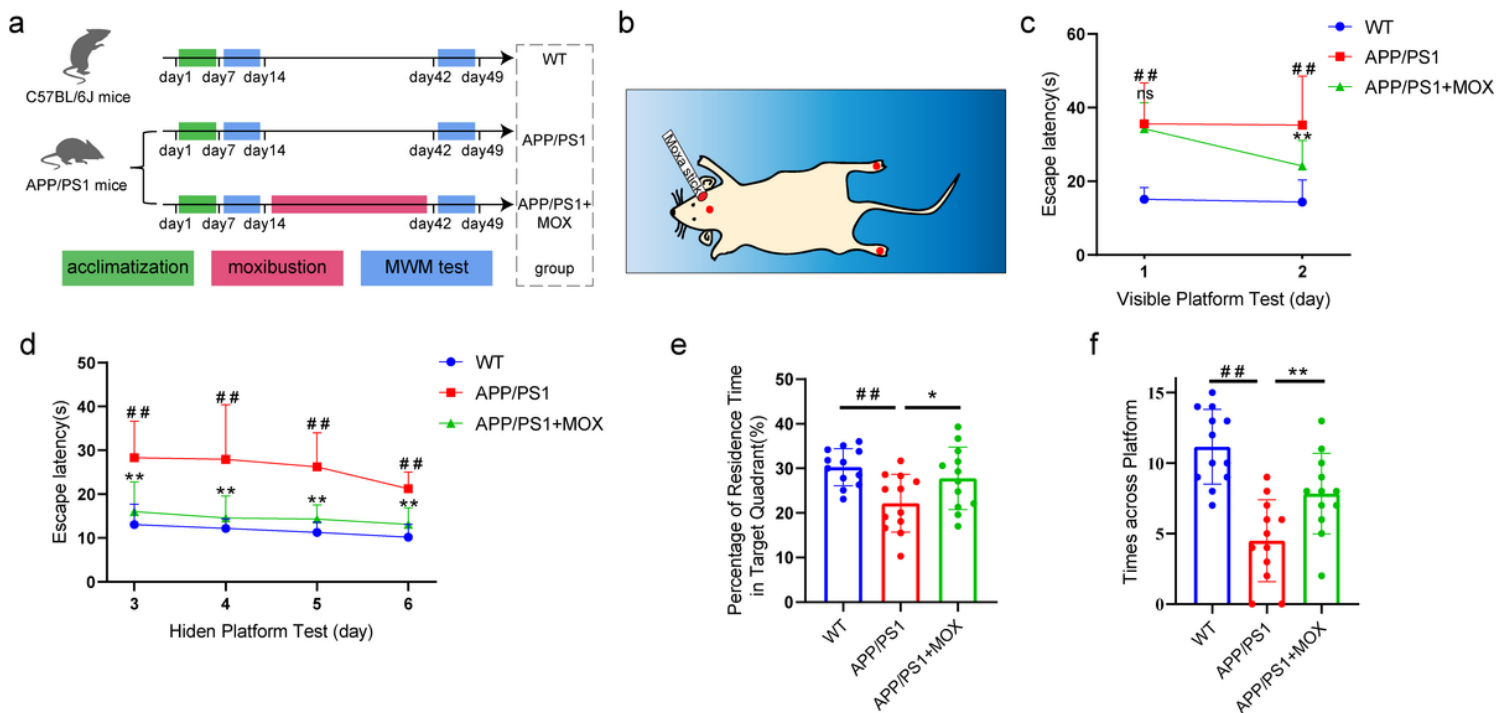


Figure 1

Water maze experiment showed the therapeutic effect of moxibustion. (a) Flow chart of the experiment. Water maze test was carried out at the mice age of 5 months old. After 7 days of water maze test, the mice were treated for 4 weeks continuously, and then the water maze test was conducted again. (b)

Schematic of the locations of the acupoints in mice. The red dot on head of the mouse is GV20 acupoint and the foot center is KI1 acupoint. (c, d). Learning curves of Ctrl (blue), APP/PS1 (red) and APP/PS1+MOX (green) mice in MWE test with visible (c) and hidden (d) platform. (e, f) Percentage of residence time in target quadrant (e) and crossing platform times (f) of Ctrl (blue), APP/PS1 (red) and APP/PS1+MOX (green) mice. One-way ANOVA test with posttest # $P < 0.05$, ## $P < 0.01$ APP/PS1 vs. WT; * $P < 0.05$, ** $P < 0.01$ APP/PS1+MOX vs. APP/PS1; ns. $P > 0.05$.

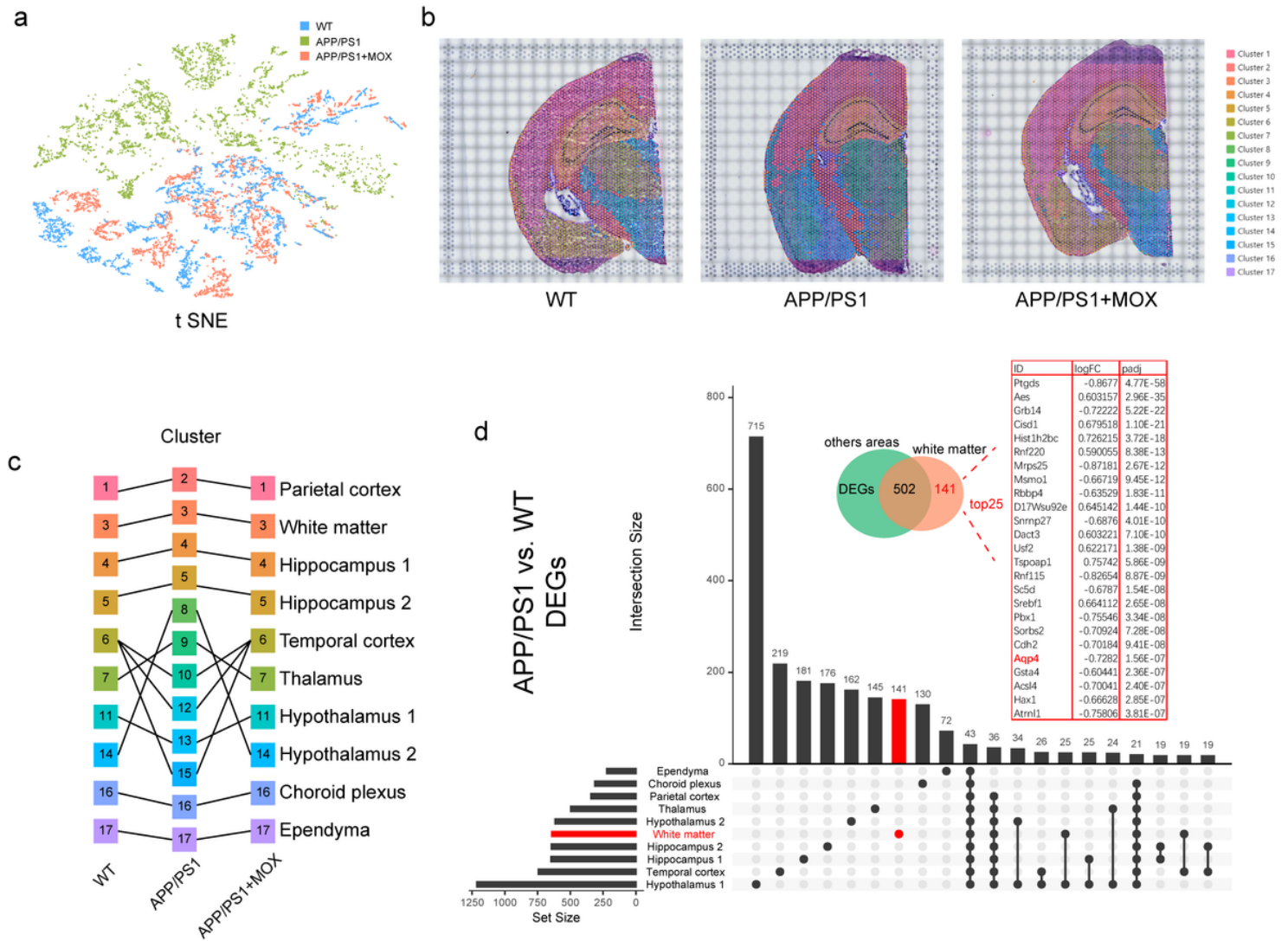


Figure 2

The expression of *Aqp4* was the highest in ependyma. (a) T-SNE plot shows the differences between the four groups. There was more overlap between APP/PS1+MOX (red) and WT (blue), but APP/PS1 (green) is relatively separate. (b) Cluster graph in each sample obtained by Graph-based. Different colors corresponded to different Clusters. (c) Schematic diagram of the relationship between cell clusters and the physiological structures of the brain. (d) UpSet plot of differentially expressed genes. The 141 differentially expressed genes (DEGs) marked in red were unique to white matter, and the list showed the top 25 DEGs sorted by *Padj*.

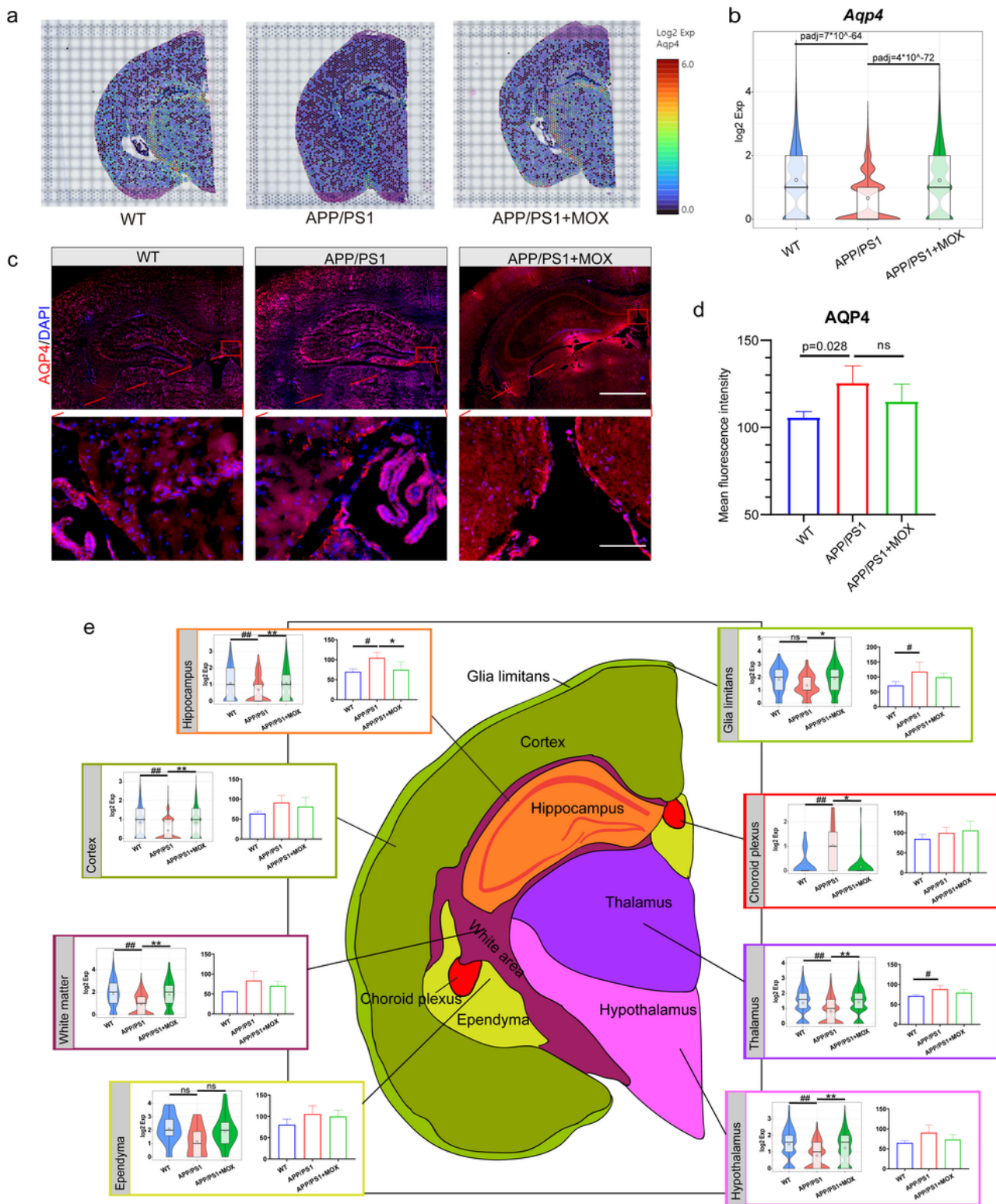


Figure 3

AQP4 differently expressed in whole brain and different brain regions. (a) The expression map of *Aqp4* in the brain. (b) Violin plot of whole brain expression of *Aqp4* in ST. Box plots elements were defined as follows: center line: median; box limits: upper and lower quartiles; circles: mean level. (c) Immunofluorescence (IF) analysis using AQP4 antibody of brain. Blue, DAPI; red, AQP4. Scale bar, 1mm; 0.1mm. (d) Bar plot showed *Aqp4* expression of whole brain in IF. Used one-way analysis of variance. (e)

The brain was divided into glia limitans, cortex, white matter, hippocampus, thalamus, hypothalamus, ependyma and choroid plexus, and the expression levels of different brain regions in ST and IF were counted and compared between groups. The violin graph showed the ST data, and the bar chart showed the IF data. P-value from edgeR analysis in ST and one-way analysis of variance with posttest p-value in IF: # $P < 0.05$, ## $P < 0.01$ APP/PS1 vs. WT; * $P < 0.05$, ** $P < 0.01$ APP/PS1+MOX vs. APP/PS1; ns $P > 0.05$. N = 3 for all groups in IF.

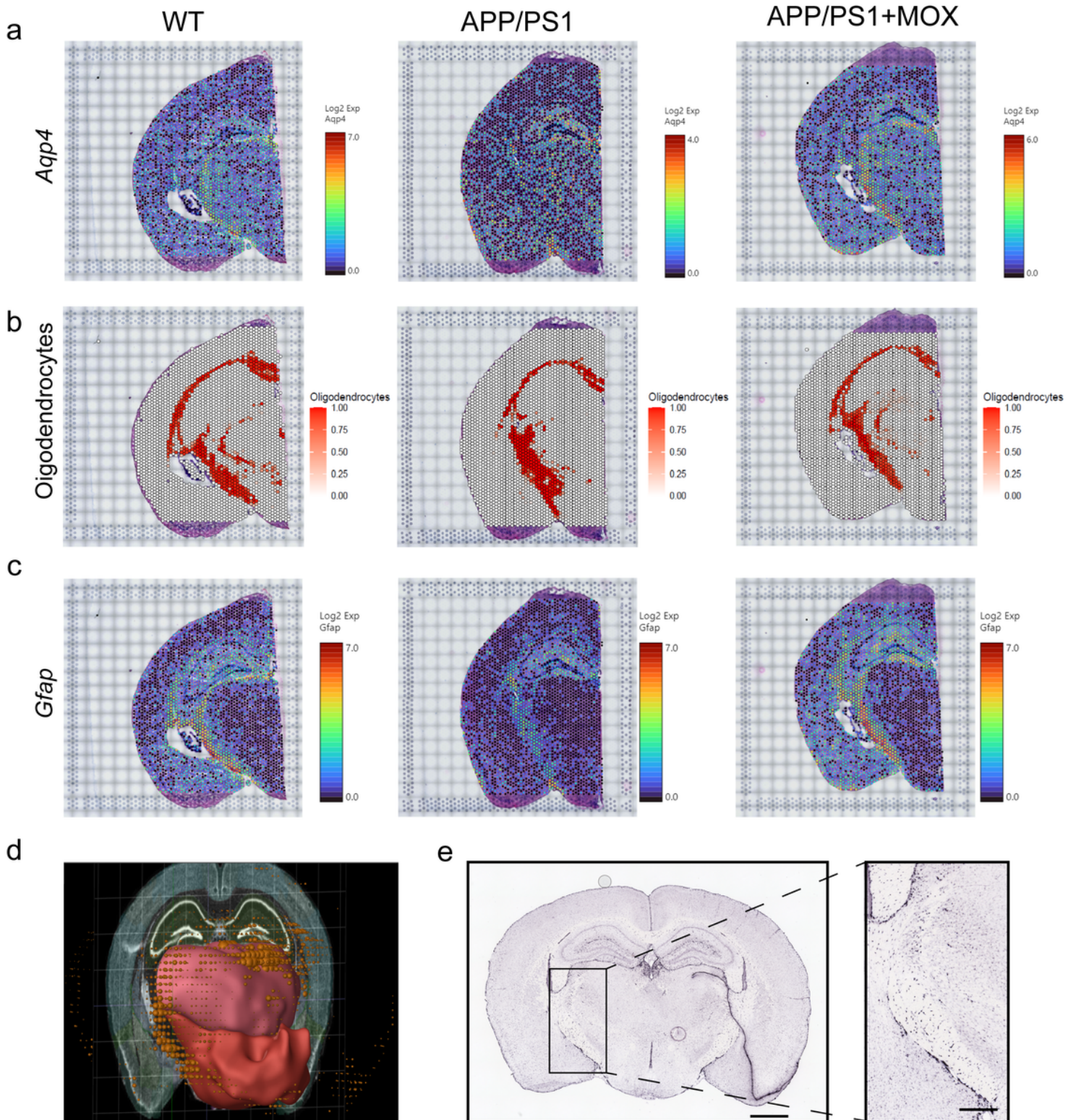


Figure 4

Differential distribution of *Aqp4* in white matter areas. (a) The *Aqp4* expression map with own scale bar. (b) Distribution and richness map of oligodendrocytes cells annotated by single cell sequencing data. The corresponding value of its color was the proportion of the cell's genes in all genes in spots. (c) The expression map of *Gfap* in the brain, which had high expression in the white matter region in map. (d-e) 3D(d) and sectional(e) distribution of *Aqp4* RNA around the thalamus and hypothalamus by in situ hybridization (ISH) from Allen Mouse Brain Atlas. The red structure represented the hypothalamus, the pink structure represented the thalamus, the orange dot represents *Aqp4* mRNA, and the size of the dot is the amount of expression. Scale bar, 1mm; 0.4mm. For the 3D images in **d**, brain are captured from the Allen Institute for Brain Science's Mouse Brain Atlas[17] (© 2004 Allen Institute for Brain Science, Allen Mouse Brain Atlas available from: mouse.brain-map.org/) using Brain Explorer®2[23]

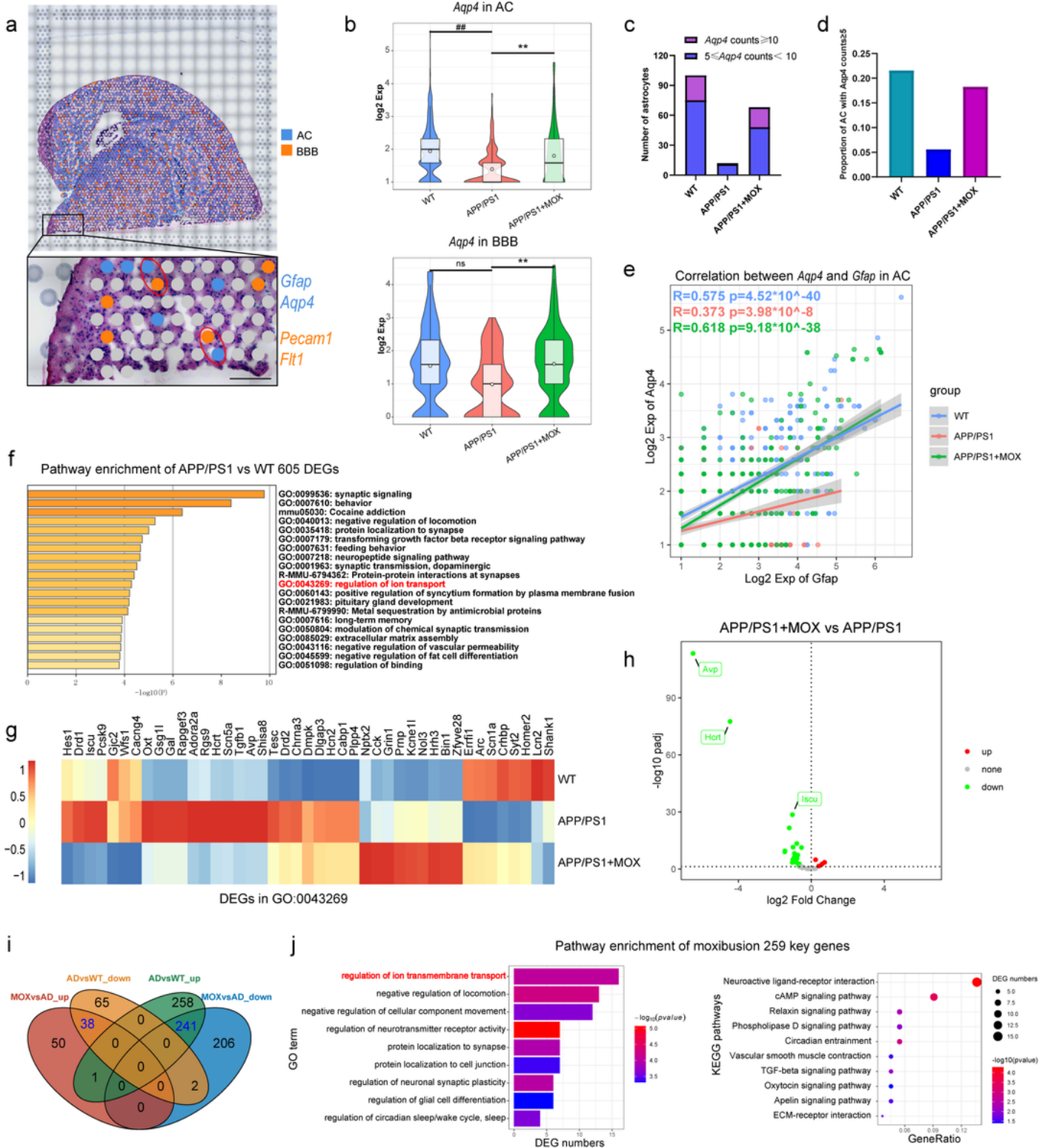


Figure 5

Spatial transcriptomics analysis of perivascular astrocytes. (a) Schematic diagram of screening methods for perivascular astrocytes. *Gfap*, *Aqp4* represent the signature genes of astrocyte, while *Pecam1* and *Flt1* represent the signature genes of blood vessels. Orange and blue points represent BBB and astrocytes (AC). (b) Violin plots of *Aqp4* expression in BBB and AC between groups. P-value from edgeR analysis: ## $P < 0.01$ APP/PS1 vs. WT; * $P < 0.05$, ** $P < 0.01$ APP/PS1+MOX vs. APP/PS1; ns $P > 0.05$. (c)

Stacked bar charts indicating the number of AC with high *Aqp4* expression in each group. (d) A bar chart showing the proportion of AC in which the counts of *Aqp4* expression are greater than 5. (e) A scatter plot with linear fit line showing the correlation between *Aqp4* expression and *Gfap* expression in each group's AC. R: Pearson's correlation coefficient, p: Pearson's correlation test p-value. (f) Bar charts about pathway analysis of the differentially expressed genes ranked between APP/PS1 and WT by using Metascape. The pathway of the red words showed the pathway with a close relationship to *Aqp4*. (g) A heat map showing the expression in three groups of APP/PS1 vs. WT DEGs enriched to the regulation of ion transport (GO: 0043269). (h) Volcano plots presenting the differentially expressed genes in **g** between APP/PS1+MOX and APP/PS1. The dotted lines perpendicular to the horizontal axis and perpendicular to the vertical axis represented Fold Change = 0 and *P*_{adj} = 0.05. (i) Venn plot of key genes of moxibustion. 38 up-regulated genes and 241 down-regulated genes (the blue numbers in the figure) were potential target key genes. (j) Barplot of representative GO terms and bubble plot of the enriched KEGG pathways.

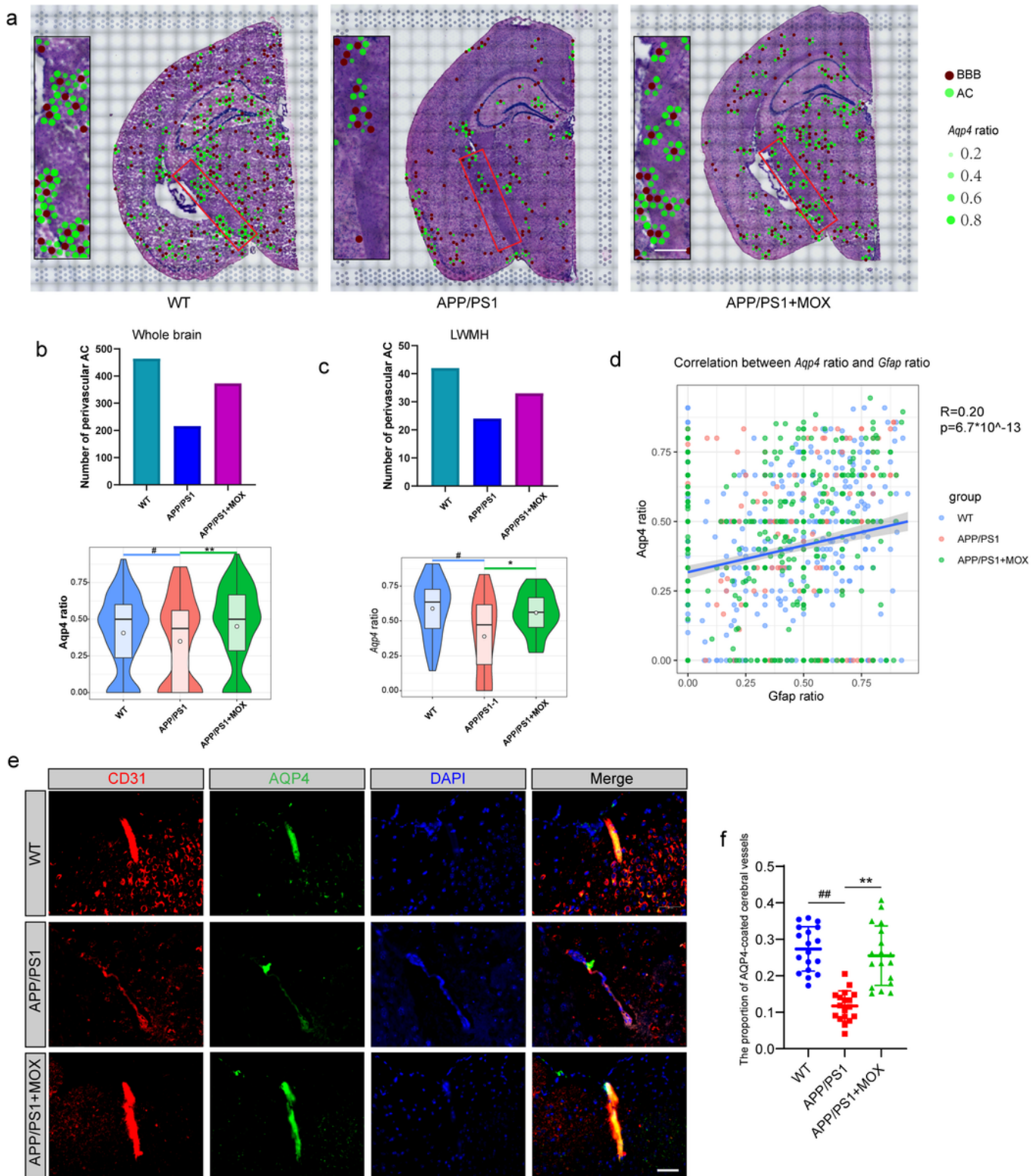


Figure 6

Analysis of *Aqp4* accumulation in perivascular astrocytes endfoot. (a) Brain maps of *Aqp4* ratio. The *Aqp4* ratio in AC represented the degree of *Aqp4* concentration in the AC endfoot in BBB. The brown points represented BBBs, and the green points represented ACs. The size and alpha of the green points represented the magnitude of the *Aqp4* ratio. The enlarged area was LWMH. Scale bar, 0.3mm. (b, c) Barplot of the number of perivascular AC and violin plots of *Aqp4* ratio in brains (b) and LWMH (c). (d) A

scatter diagram showing the correlation between *Aqp4* ratio and *Gfap* ratio in AC. R: Pearson's correlation coefficient, p: Pearson's correlation test p-value. (e) IF analysis using CD31 and AQP4 antibody of brain. Blue, DAPI; red, CD31; green, AQP4. Scale bar, 40µm. (f) Dot plot of the proportion of AQP4-coated cerebral vessels (N = 18). One-way analysis of variance with posttest #*P* < 0.05, ##*P* < 0.01 APP/PS1 vs. WT; **P* < 0.05, ***P* < 0.01 APP/PS1+MOX vs. APP/PS1.

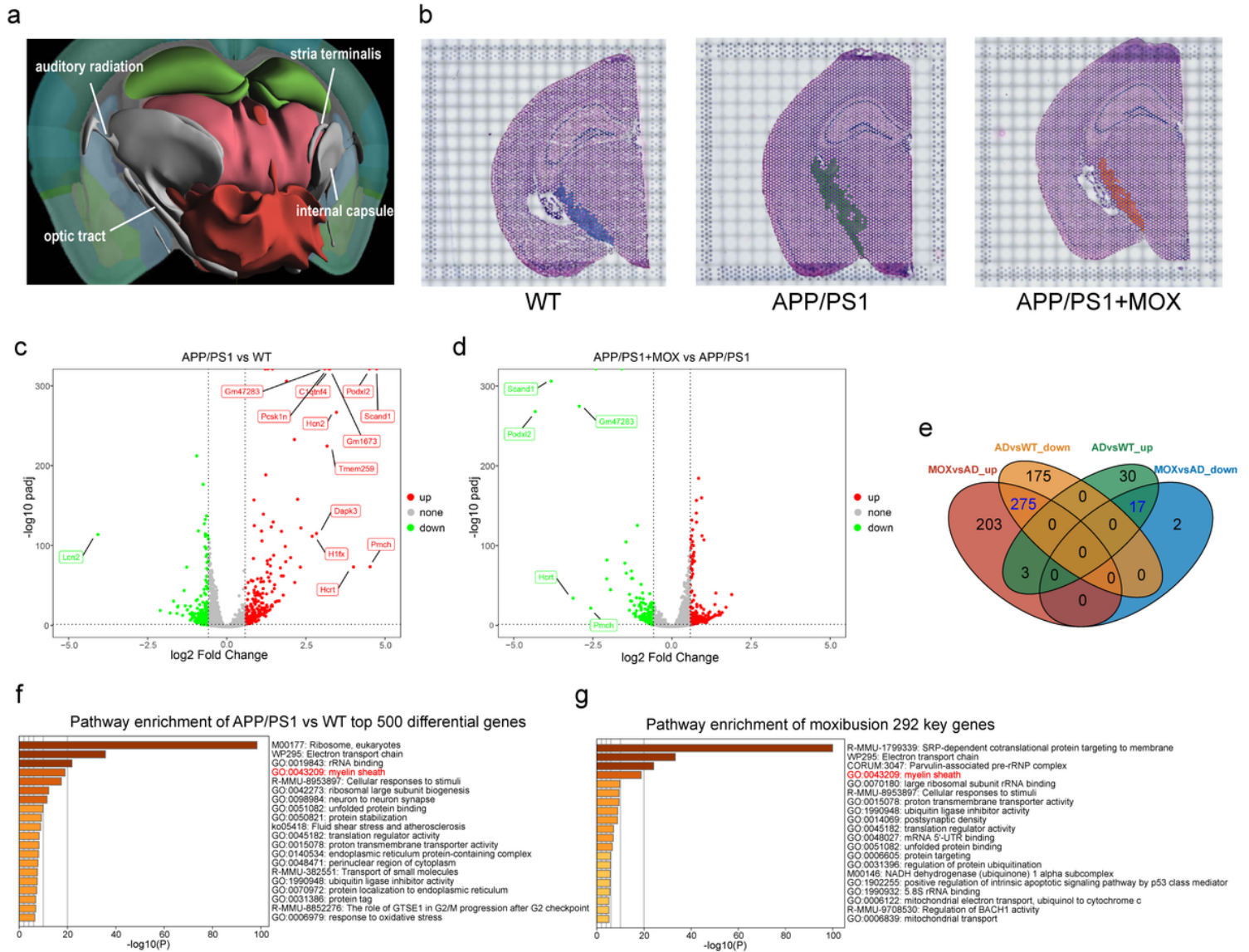


Figure 7

Spatial transcriptomics analysis of LWMH. (a) A schematic diagram of the physiological structure of the LWMH. The gray structure represented the internal capsule, stria terminalis, auditory radiation and the optic tract. (b) LWMH sampling maps. The color area in the pictures was the selected area. (c, d) Volcano plots presenting the differences between APP/PS1 and WT (c), APP/PS1+MOX and APP/PS1 (d) in LWMH. The dotted lines perpendicular to the horizontal axis and perpendicular to the vertical axis represented Fold Change = -1.5, Fold Change = 1.5 and *P*_{adj} = 0.05. (e) Venn plot of key genes of moxibustion. The blue numbers in the figure were the target number of key genes. (f, g) Bar charts about

pathway analysis of the DEGs ranked by using Metascape. For the 3D images in **a**, brain are captured from the Allen Institute for Brain Science's Mouse Brain Atlas (© 2004 Allen Institute for Brain Science, Allen Mouse Brain Atlas available from: mouse.brain-map.org/) using Brain Explorer®2[23]

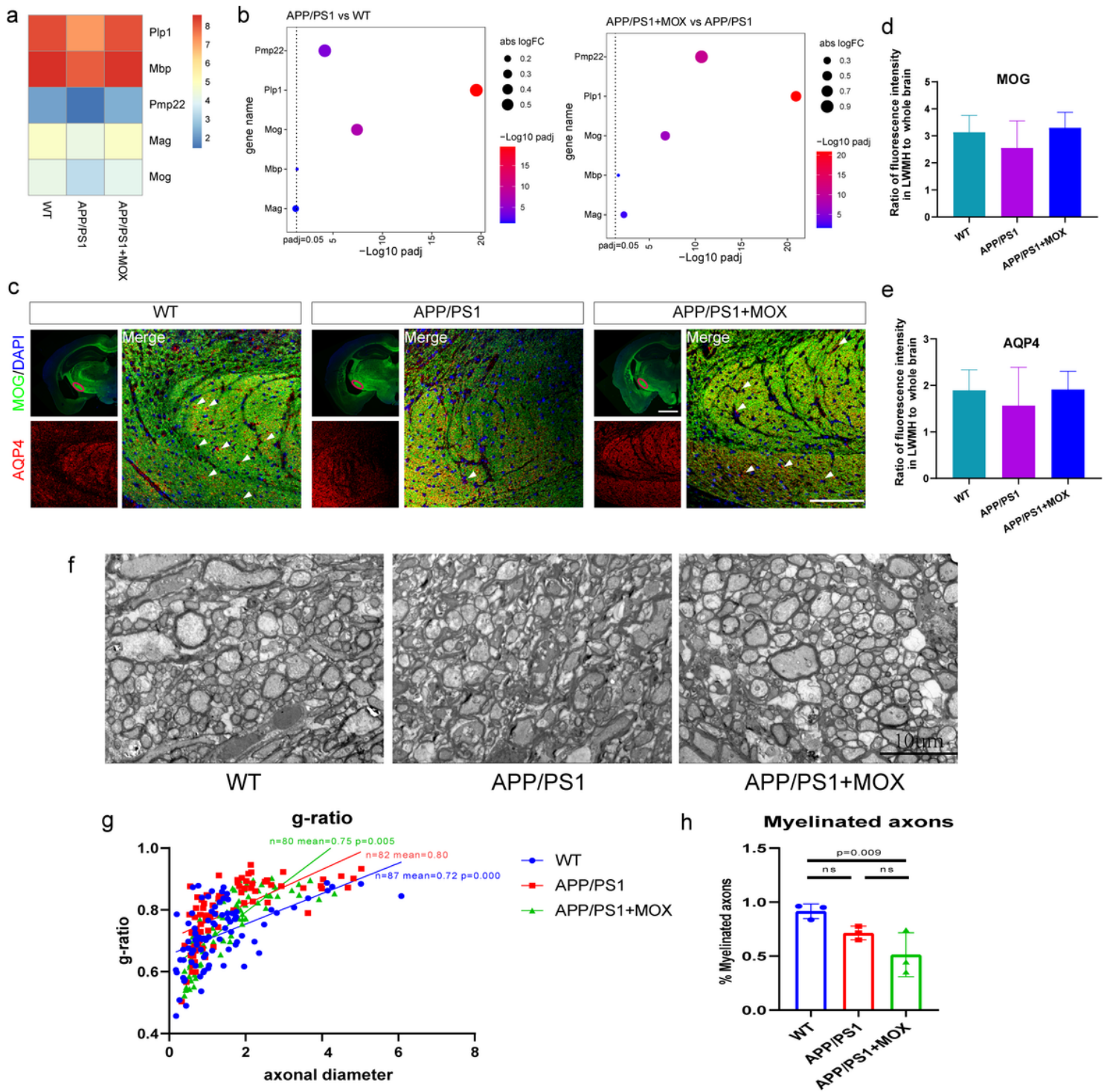


Figure 8

Analysis of myelin sheath injury in LWHT. (a) Heat map of genes expression of five myelin structural proteins in three groups. The value corresponding to the icon was log2 expression. (b) The bubble chart

shows the difference of genes between two samples. The size of the bubble represented the Fold Change, and the color represents the size of the *Padj* by edgeR. (c) IF analysis using MOG antibody of brain. The enlarged area was LWMH. The white arrow pointed to the thicker fibrous astroglia processes. Blue, DAPI; green, MOG; red, AQP4. Scale bar, 1mm, 0.1mm. (d) Bar plot of ratio of fluorescence intensity of MOG in LWMH to whole brain in IF. (N = 3, ns.) (e) Bar plot of ratio of fluorescence intensity of AQP4 in LWMH to whole brain in IF. (N = 3, ns.) (f) Transmission electron microscopy images of the optic tract (Magnification $\times 1,500$). Scale bar, $10\mu\text{m}$. (g) The g-ratio of the myelin of the mice was measured. They were measured as the axon diameter/total diameter of the axon plus the myelin sheath. (h) The percentage of myelinated axons was quantified. Used one-way analysis of variance with posttest in figures **g** and **h**.

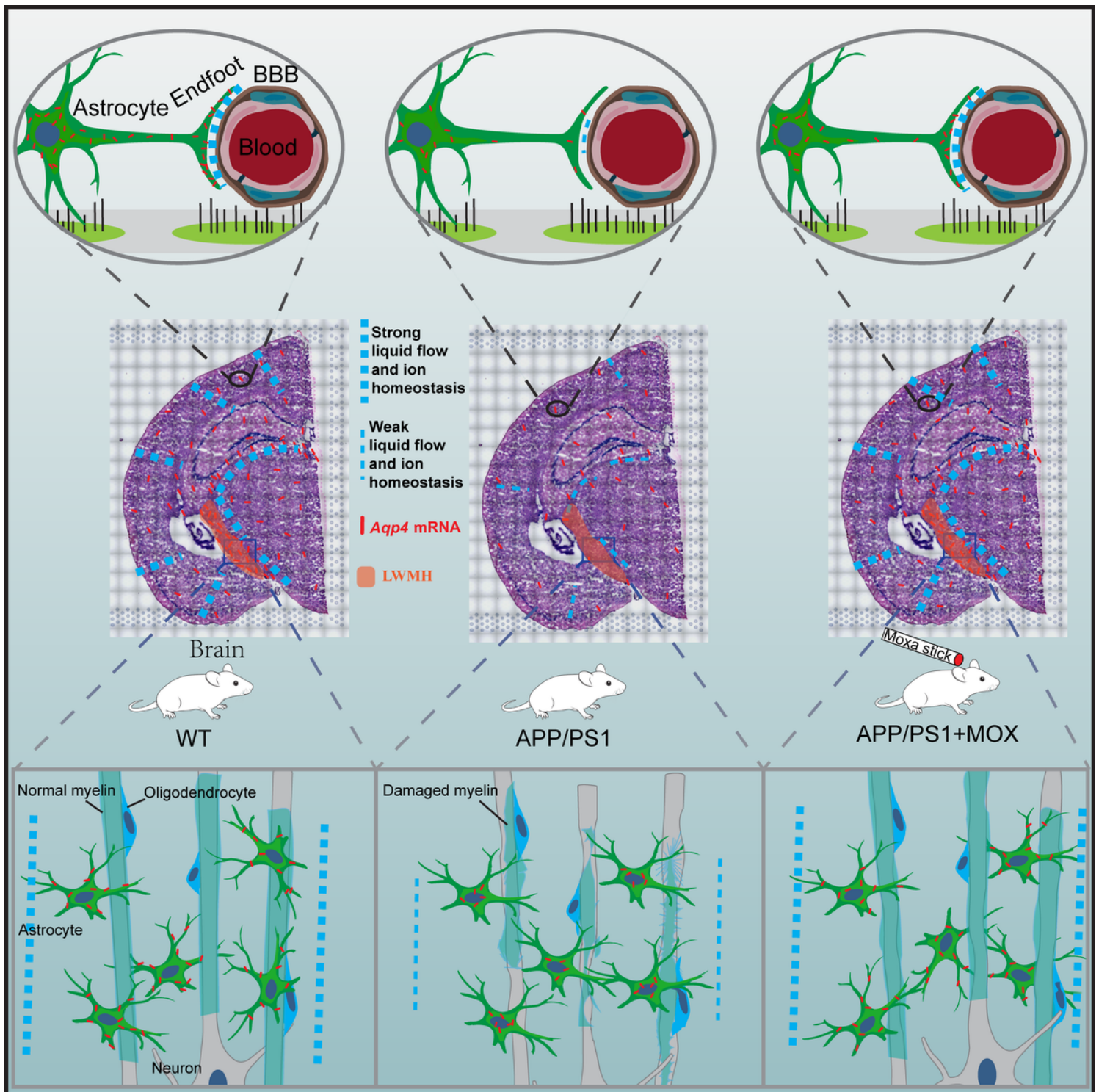


Figure 9

The scheme of the study. Under healthy conditions, astrocytes transport *Aqp4* mRNA to processes or endfeet, causing the translated AQP4 proteins to gather at the site of action. And the normal expression of AQP4 can maintain strong liquid flow and ion homeostasis. Throughout the brain, astrocytes express a large amount of AQP4 around the cerebral vessels and in LWMH. However, in APP/PS1 mice, the ability of astrocytes to transport *Aqp4* mRNA decreased, which prevented AQP4 from being localized in astrocyte processes or endfeet. This change leads to the weakening of the liquid flow in the space around

the cerebral vessels, which not only affects the normal function of the BBB, but also makes the glial-lymphatic system dysfunction. In LWMH, there was also a decrease in the astrocytes *Aqp4* expression in APP/PS1 mice, which reduced the supply of oligodendrocytes, disturbed the ion homeostasis and promoted the damage of myelin sheath. After moxibustion on APP/PS1 mice, the ability of astrocytes to transport *Aqp4* mRNA was improved, the *Aqp4* expression in LWMH increased and myelin renewal was promoted.